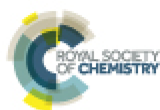

Sustainable
Energy & Fuels

# Energetic Effects of Hybrid Organic/Inorganic Interfacial Architecture on Nanoporous Black Silicon Photoelectrodes

| | |
|---|---|
| Journal: | *Sustainable Energy & Fuels* |
| Manuscript ID | SE-ART-01-2019-000032.R1 |
| Article Type: | Paper |
| Date Submitted by the Author: | 27-Feb-2019 |
| Complete List of Authors: | Pekarek, Ryan; National Renewable Energy Laboratory; The University of Texas at Austin<br>Christensen, Steven; NREL,<br>Liu, Jun; National Renewable Energy Laboratory<br>Neale, Nathan; National Renewable Energy Laboratory, |
| | |

SCHOLARONE™
Manuscripts

Journal Name

ARTICLE

# Energetic Effects of Hybrid Organic/Inorganic Interfacial Architecture on Nanoporous Black Silicon Photoelectrodes†

Received 00th January 20xx,
Accepted 00th January 20xx

DOI: 10.1039/x0xx00000x

**www.rsc.org/**

Ryan T. Pekarek[1,2], Steven T. Christensen[3], Jun Liu[3], Nathan R. Neale[1*]

Photoelectrochemical cells have been the subject of great interest in the research community as a route for fuel formation directly from sunlight. Interfacial layers are frequently employed on the surface of light-absorbing semiconductor photoelectrodes to enhance the activity and stability of the semiconductor. Here we consider the energetic effects of such layers on a nanoporous 'black' silicon photocathode. We construct hybrid organic/inorganic films by growing an oxide-nucleating molecular monolayer on the nanostructured Si surface and burying this molecular monolayer under $TiO_2$ deposited by atomic layer deposition. We examine the energetic effects of this hybrid interfacial architecture via our recently developed intensity-modulated high-frequency resistivity (IMHFR) impedance spectroscopy technique and quantify the change in thermodynamic flatband potential as the oxide thickness is increased from 0–15 nm. By comparing the IMHFR data with traditional voltammetry, we are able to deconvolute the thermodynamic and kinetic contributions that determine the observed proton reduction onset potential. We also study these photoelectrodes with Pt nanoparticles either (i) deposited on top of the molecular/$TiO_2$ interfacial layer or (ii) etched into the Si surface. In the first architecture, a beneficial positive shift in the thermodynamic flatband potential is achieved from the Si|molecular|$TiO_2$ *p-n* junction, but the lack of a direct Si|Pt contact results in large kinetic charge transfer losses. In contrast, the second architecture allows for facile charge transfer due to the direct Si|Pt contact but negates any benficial thermodynamic effect of the molecular/$TiO_2$ bilayer. Despite the lack of thermodynamic effect of the hybrid molecular/$TiO_2$ interfacial layer, we find that there is still a significant kinetic benefit from this layer. This work demonstrates the sensitive nature of the thermodynamics and kinetics on the interfacial architecture and yields critical insights into the design of photoelectrochemical interfaces.

## Introduction

Photoelectrochemically driven reactions are an attractive approach to capture and store solar energy.[1] The quest for an efficient and robust solar fuel-forming device based on a direct semiconductor|electrolyte junction motivates the development of increasingly complex semiconductor surface architectures with correspondingly intricate interfacial energetics. Organic and inorganic modifications of semiconductor photoelectrodes have been explored extensively and each are known to profoundly affect photoelectrochemical performance. What is less frequently understood is how each component affects the overall system's thermodynamics and kinetics, especially in complex hybrid organic/inorganic interfacial architectures. Consequently, deconvoluting the energetic effects that occur as a result of each interfacial component at the semiconductor|liquid junction is a critical research objective that will enable rationally designed interfaces.[2,3]

The prototypical protection strategy for semiconductor-based photoelectrochemical cells is to deposit inorganic oxide layers such as titania ($TiO_2$) layers onto the semiconductor surface.[4–17] In addition to providing a corrosion barrier between the semiconductor and the electrolyte, the electronic structure of the oxide plays a key role in the interfacial energetics. On $GaInP_2$, for example, inherently *n*-type $TiO_2$ facilitates charge separation at the *p-n* junction formed by the two semiconductors and provides a thermodynamic energy barrier to recombination.[3] Under illumination, photoexcited electrons move into the $TiO_2$, spatially separating them from the holes that remain in the underlying semiconductor and providing an additional (kinetic) energetic barrier to recombination.[3]

In addition to inorganic layers, the presence of a molecular moieties bound to a photoelectrode provides additional functionality to surface. The molecular dipole on the surface forces the semiconductor to equilibrate to an additional electric field, shifting the interfacial energetics.[18–21] Silicon(111) has been functionalized with various organic molecules (alkyl,[22] aromatic,[19] fluorinated[21]) and halogens[23,24] where the effect of the dipole has been measured electrochemically and/or spectroscopically. Similar studies have been performed on

[1]Chemistry and Nanoscience Center, National Renewable Energy Laboratory, 15013 Denver West Parkway, Golden, Colorado 80401, United States
[2]Department of Chemistry, The University of Texas at Austin, 2506 Speedway STOP A5300, Austin, Texas 78712, United States
[3]Materials Science Center, National Renewable Energy Laboratory, 15013 Denver West Parkway, Golden, Colorado 80401, United States
*Corresponding author email: nathan.neale@nrel.gov
†Electronic Supplementary Information (ESI) available: See DOI: 10.1039/x0xx00000x

This journal is © The Royal Society of Chemistry 20xx


Please do not adjust margins

Si(100)[20] and silicon microwires.[25] In addition to the electronic effects, molecular surface functionalization can also slow substrate oxidation[26–28] and control surface wetting.[29,30] Incorporating molecular moieties on the surface also is known to tune the (electro)chemical reactivity of the semiconductor surface for fuel-forming reactions[7,31–37] and other reversible redox couples.[38–45] Of direct relevance to this study, molecular species additionally can serve as nucleation sites for metal oxide growth via atomic layer deposition (ALD) and facilitate clean semiconductor/metal oxide junctions.[46]

Previous work on planar Si(111) demonstrated that the formation of hybrid organic/inorganic films can accrue the benefits of each component, where the effect of the organic molecular dipole was observed through the ultrathin (~2 nm) $TiO_2$ and produced significant positive shifts in the proton reduction onset potential ($V_{onset}$).[19] Previous work on nanoporous 'black' silicon (*b*-Si), prepared by metal-assisted chemical etching (see experimental details), is an exciting alternative to traditional planar silicon wafers since *b*-Si features a high surface area that promotes gas bubble desorption and thus enables large photocurrent densities[47–49] while leveraging the same appealing features as planar Si (optimal bottom cell band gap of ~1.1 eV, high natural abundance, and industrial maturity).[50]

Here, we apply a hybrid organic/inorganic interfacial architecture to *b*-Si and reveal intriguing insights into the thermodynamic and kinetic energetics resulting from this bilayer structure both with and without platinum nanoparticle (Pt NP) catalysts. The baseline hybrid organic/inorganic architecture is comprised of $TiO_2$|1,4-butanediol|*b*-Si formed by reacting 1,4-butanediol with the nanoporous *b*-Si and then growing $TiO_2$ on top of this molecularly-functionalized semiconductor using ALD. We modify these baseline hybrid architectures with Pt NPs either buried into the *b*-Si or deposited on top of the $TiO_2$ and (photo)electrochemically probe the junction energetics of these two systems as a function of $TiO_2$ thickness. In addition to traditional voltammetric studies of the nanoporous films where we measure $V_{onset}$, which represents a summation of the interfacial thermodynamics and kinetics, we also isolate the former as flatband potential ($V_{fb}$) through our recently-developed impedance technique called intensity-modulated high frequency resistivity (IMHFR) spectroscopy.[51] By subtracting $V_{onset}$ from $V_{fb}$, we separate the kinetic losses from the system thermodynamic potential and report a kinetic overpotential, $\eta_{kin}$. These studies provide a comprehensive analysis of the kinetic and thermodynamic contributions of hybrid organic/inorganic architectures and Pt NP catalysts to the photoelectrochemical behavior of nanoporous black silicon and serve as a guide for future investigations of hybrid organic/inorganic interfacial concepts.

## Results and Discussion

### Organic Monolayer Formation

Nanoporous *b*-Si is prepared via a metal-assisted chemical etch (MACE) on *p*-Si(100) by a previously reported procedure.[47,49] To prepare the first architecture, termed 'surface Pt', we bind a molecular monolayer to to the Pt-free *b*-Si surface followed by ALD $TiO_2$, and then deposit Pt NPs on top of this organic/inorganic hybrid bilayer via ALD. In the second architecture, termed 'buried Pt', we etch electrolessly deposited Pt NPs into the pre-formed *b*-Si wafer via a brief secondary MACE step. We then bind the same molecule to the Pt NP-embedded silicon followed by ALD $TiO_2$. These two architectures are juxtaposed in Scheme 1.

**Scheme 1** Two architectures studied in this work: 'Surface Pt' (Pt/$TiO_2$/diol/*b*-Si) and 'Buried Pt' ($TiO_2$/diol/B-Pt/*b*-Si).

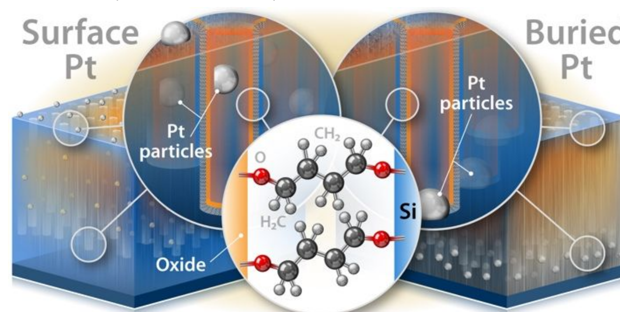


We required a molecule with two functional groups to bind both the silicon and nucleate the growing oxide during ALD, and a symmetric molecule was chosen to avoid non-selective attachment. Given these constraints, the molecular species 1,4-butanediol was selected and tethered via an alkoxy linkage to the *b*-Si surface by a radical-initiated binding process we previously developed for chemisorbing functional groups to silicon nanoparticles (Scheme S1).[52] Since the anti-reflectivity and porosity of *b*-Si complicate spectroscopic characterization of the monolayer deep in the pores (*e.g.*, reflectance-based techniques suitable for wafer samples are not possible), we confirmed successful monolayer formation electrochemically using a redox-active reporter molecule. A Steglish condensation was performed between ferrocenecarboxylic acid and the terminal alcohol group in the molecularly-functionalized *b*-Si (Scheme S1). We then collected cyclic voltammograms and quantified molecular coverage using the linear relationship between peak current and scan rate. We also performed the same chemistry on a planar Si(100) wafer to compare the electrochemically active surface area between the geometric and projected surfaces.

Figure 1 depicts voltammograms in nonaqueous electrolyte (0.2 M $LiClO_4$ in MeCN) at multiple scan rates for planar silicon as the baseline. In the planar case (Figure 1a), the potential separation between anodic and cathodic peaks is small and the peak current ($j_p$) is linear with scan rate, indicating a surface-bound redox moiety. The calculated coverage ($0.6 \times 10^{14}$ molecules/$cm^2$) is similar to several reports bonding vinylferrocene to *p*-Si(100) where a range of $0.4–1.4 \times 10^{14}$ molecules/$cm^2$ was observed.[40,43,45,53,54] As expected, molecular surface coverage significantly rises after nanostructuring (Figure 1b). The Steglish ferrocene coverage on *b*-Si is $5.7 \times 10^{14}$ molecules/$cm^2$, nearly double the expected ~5-fold increase in geometric surface area of *b*-Si compared with planar silicon.[55,56]


This journal is © The Royal Society of Chemistry 20xx

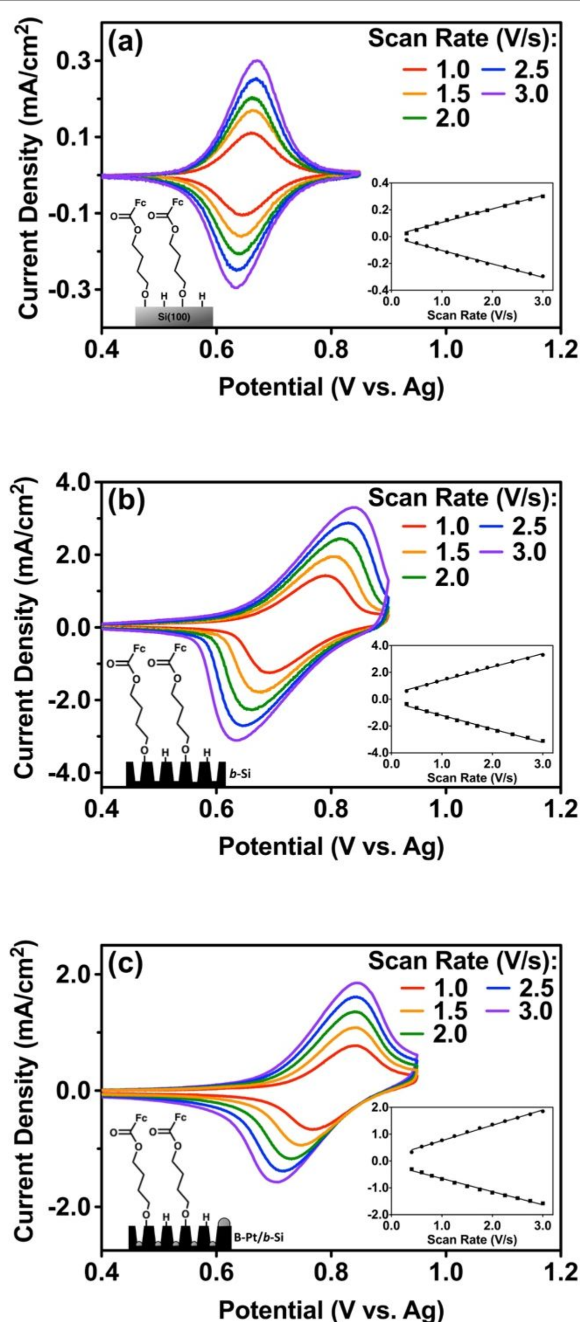


**Fig. 1** Cyclic voltammograms at various scan rates of (a) planar diol/Si(100), (b) diol/*b*-Si, and (c) diol/B-Pt/*b*-Si photoelectrodes after Fc-COOH esterification. (d) Summary of coverages measured in this work. Conditions: 0.2 M LiClO4 in MeCN.

One explanation for the greater than expected coverage is that the nanostructured geometry allows for greater packing of large ferrocene molecules. Another possible explanation is that the mixed surface hydrides $*SiH_x$ (where *Si indicates a Si surface atom) on the *b*-Si nanoporous layers are more amenable to radical reactions than the $*SiH_2$ groups at the Si(100) planar wafer, as has been seen for Si nanoparticles containing monohydride *SiH (similar to Si(111) surfaces), dihydride $*SiH_2$, and trihydride (silyl) $*SiH_3$ surface groups.[57] A control experiment with directly-bound Fc-COOH (*i.e.*, Steglish condensation without the alkoxy monolayer) achieves just $0.9 \times 10^{14}$ molecules/cm$^2$ on *b*-Si. Thus, this ferrocene reporter molecule method is a valid representation of 1,4-butanediol monolayer coverage as relatively little ferrocene binds without the pre-adsorbed monolayer. Another interesting conclusion is that bidentate diol binding must be minimal, otherwise the Steglish condensation would not work and the directly-bound Fc-COOH and Steglish Fc-COOH coverages would be the same. Therefore, we conclude that the terminal alcohol remains exposed after binding and should facilitate ALD oxide nucleation. Finally, we studied how nanostructuring affects the cyclic voltammogram peak currents and shapes. While the peak current remains linear with scan rate upon nanostructuring, the peak potentials are more separated in molecularly-functionalized *b*-Si compared with planar silicon. This shape is likely a product of slower electrolyte diffusion through the pores or a slight decrease in the electron transfer kinetics across the *b*-Si|electrolyte interface. Similar phenomena have been observed on ferrocene-functionalized silicon microwires.[38]

When Pt NPs are buried into the nanoporous silicon (B-Pt/*b*-Si) via a secondary metal-assisted chemical etch followed by diol attachment, the peak shape is similar to that of *b*-Si, suggesting that Pt deposition does not significantly affect the nanostructured surface – consistent with our prior report.[49] However, the peak current is roughly halved resulting in a significant decrease in calculated surface coverage ($3.1 \times 10^{14}$ molecules/cm$^2$). This decrease is likely due to the Pt NPs either blocking silicon sites or interfering with the monolayer formation reaction. For example, electroless deposition of Pt NPs proceeds via a galvanostatic reaction and could lead to surface reconstruction that would change the available $*SiH_x$ binding sites, adversely affecting the radical reaction.

## $TiO_2$ Deposition and Interfacial Architecture

### Imaging Titania Depsotion on Nanoporous Silicon

We next studied the deposition of $TiO_2$ via ALD onto 1,4-butanediol-functionalized *b*-Si. To minimize silicon oxidation, the wafer was transferred to the ALD chamber directly from a glovebox via an air-free load-lock. The deposition chamber was heated to 200 °C to decrease the defect density in the oxide film without degrading the monolayer. To understand the morphology of the oxide layer on the nanoporous substrate, we took cross-sectional STEM-bright field (BF) images of a portion of the sample. Figure 2 depicts STEM-BF and STEM-electron energy loss spectroscopy (EELS) images after 200 $TiCl_4/H_2O$ ALD cycles. The pores are ~750 nm deep, 40–50 nm wide with a high pore density, all of which are consistent with our previous reports on *b*-Si.[48,49] The Ti-$L_{2,3}$ and O-K edges were used to obtain the EELS spectral images to see the distribution of Ti and O atoms. The EELS images of Ti (red) and O (green) reveal that the $TiO_2$ deposits into the entire length pores. For simplicity throughout this work we label the $TiO_2$ thickness of each sample with the thickness determined by the same number of ALD cycles on planar, native oxide-coated silicon(100) wafer.

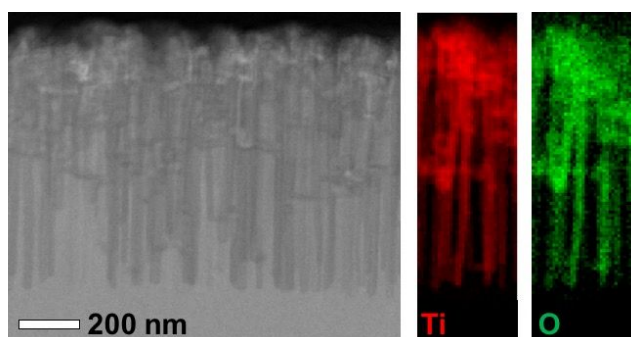


**Fig. 2** Scanning TEM images of the $TiO_2$/diol/*b*-Si where 200 cycles (~10 nm) $TiO_2$ were deposited. Left to right: STEM-BF image, EELS images of titanium (red) and oxygen (green).

**Electrochemical Characterization of the Surface Pt Architecture**

We complete the photoelectrochemical interface with the deposition of catalytic Pt nanoparticles onto the surface of the ALD-deposited $TiO_2$. To probe the role of $TiO_2$ in this hybrid organic/inorganic interfacial architecture, we collected voltammograms in 0.5 M $H_2SO_4$ as a function of $TiO_2$ thickness (Figure 3) and extracted the proton reduction onset potential ($V_{onset}$) as the potential where the current is –1 mA/cm$^2$. When just 2.5 nm of $TiO_2$ is deposited between the *b*-Si and Pt, $V_{onset}$ is 0.22 V vs RHE. Increasing the $TiO_2$ thickness to 5 nm produces a small positive $V_{onset}$ shift, but additional $TiO_2$ beyond 5 nm results in negative shifts. Previous work demonstrated that when native $SiO_x$ is grown on unfunctionalized *b*-Si, $V_{onset}$ improves after 1 h of air exposure but decreases after longer times.[48] As the native oxide thickness is proportional to time in air, our results correlate well with this observation where a small amount of oxide (here $TiO_2$) improves $V_{onset}$, but the trend reverses as the oxide thickness is increased. The region of positive current correlates well with $H_2$ oxidation and, consistent with the peak separation from the voltammograms in Figure 1, this feature may indicate that $H_2$ diffusion is slow within the pores and remains available for oxidation.

The improvement in $V_{onset}$ for thin $TiO_2$ may be due to decreased surface recombination (i.e., passivation), while the negative shifts at greater $TiO_2$ thicknesses could be a result of poor charge transfer through the oxide – both kinetic considerations. Alternatively, the silicon barrier height can move as a result of a field induced at the Si|$TiO_2$ boundary or the changes to the Helmholz layer at the $TiO_2$|solution interface – thermodynamic factors. We recently reported our use of intensity-modulated high-frequency resistivity (IMHFR) spectroscopy to show that observed changes in $V_{onset}$ are a convolution of both thermodynamic and kinetic effects.[51] Here we leverage this technique to measure the thermodynamic flatband potential ($V_{fb}$) of the samples and deconvolute the thermodynamic and kinetic factors resulting from the hybrid organic/inorganic interfacial architecture.

As we described in our recent work,[51] IMHFR simultaneously measures the light and dark space-charge resistance ($R_{SC}$) of the semiconductor photoelectrode (here Si). The high frequency (100 kHz) of the IMHFR technique shorts other circuit elements in order to focus the measurement only to $R_{SC}$, which is strongly correlated with the number of carriers at the surface. $V_{fb}$ sits at the boundary between potential regimes where photoexcited the light and dark values ($\Delta R$) yields the effect of illumination on

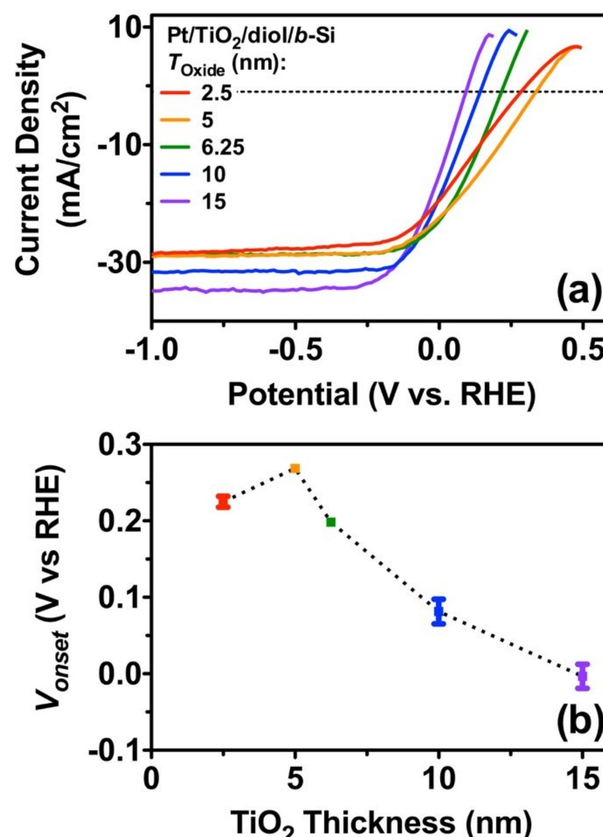


**Fig. 3** (a) Representative voltammograms for Pt/$TiO_2$ ($x$ nm)/diol/b-Si where $x$ = 2.5 (red), 5 (orange), 6.25 (green), 10 (blue), and 15 nm (purple). (b) Proton reduction onset potential ($V_{onset}$, potential where current density = –1 mA/cm$^2$) reported as a function of $TiO_2$ thickness ($T_{Oxide}$).

$R_{SC}$ as a function of potential. On *p*-type Si, when the applied carriers have a significant impact on $R_{SC}$ (depletion/inversion) and where the effect is negligible (accumulation). Subtracting potential is positive of $V_{fb}$ the majority carriers accumulate at the surface and $R_{SC}$ is predominantly governed by the hole concentration since photoexcited minority carrier (electrons) are repelled from the surface. When the applied potential is negative of $V_{fb}$ the surface is depleted of majority carriers (holes) and photoexcited electrons move to the surface where they significantly decrease $R_{SC}$. Accordingly, $V_{fb}$ is the most positive potential where photoexcited minority carriers can undergo charge-transfer at the surface and therefore represents the most postive potential where photoelectrochemical reactions are possible thermodynamically.

Figure 4a depicts the IMHFR plots for 'surface Pt' Pt/$TiO_2$/diol/*b*-Si samples where the $TiO_2$ thickness is 2.5 and 6.25 nm. It is clear from these data that Pt/$TiO_2$ films result in a much more positive $V_{fb}$ (by ~0.5 V) when the $TiO_2$ thickness is ≥ 6.25 nm. This is a very interesting observation since we showed previously that the deposition of Pt nanoparticles onto an oxide-coated silicon surface results in a negative shift in $V_{fb}$,[51]


This journal is © The Royal Society of Chemistry 20xx

and so the positive shift we observe here must be related to the $TiO_2$|diol|Si interface. This behavior may be the result of a *p-n* junction between the *p*-Si and the *n*-$TiO_2$. Considering the $V_{fb}$ as a function of $TiO_2$ thickness (Figure 4a inset), our results suggest the $TiO_2$ conduction band doesn't fully develop until the $TiO_2$ is ~ 6.25 nm thick, where the thinner layers exhibit properties uncharacteristic of bulk $TiO_2$. This hypothesis agrees well with previous spectroscopic evaluation of amorphous $TiO_2$ on $GaInP_2$, where a-$TiO_2$ thicknesses ≤5 nm do not significantly retard carrier recombination; in contrast, thicknesses greater than this value (10 and 35 nm) increase carrier lifetimes due to the 0.64 eV field at the $GaInP_2$|$TiO_2$ interface.[3]

Next, we subtract $V_{onset}$ from $V_{fb}$ to calculate the kinetic overpotential ($\eta_{kin}$) of the system and evaluate the role of interfacial kinetics in the observed proton reduction behavior. As shown in Figure 4b, with a Pt/2.5 nm $TiO_2$/diol layer, $\eta_{kin}$ is remarkably small (~0.01 V), which represents minimal kinetic overpotential from its thermodynamic value. However, $\eta_{kin}$ increases as the $TiO_2$ thickness is increased, with a large ~0.5 V barrier to charge transfer observed at 10 nm. These results suggests that the Si|diol|$TiO_2$ interface is an ideal junction (minimal kinetic overpotential) at 2.5 nm $TiO_2$ thickness. In addition, the slow electron transfer kinetics through >2.5 nm $TiO_2$ thick are quantified as a 0.15–0.5 V loss from the thermodynamic $V_{fb}$. We posit that a near ideal Si|diol|$TiO_2$ interface also occurs in the thicker $TiO_2$ samples, but that at these thicknesses, upward band-bending at the solution|$TiO_2$ interface occurs due to the *n*-type nature of the oxide.

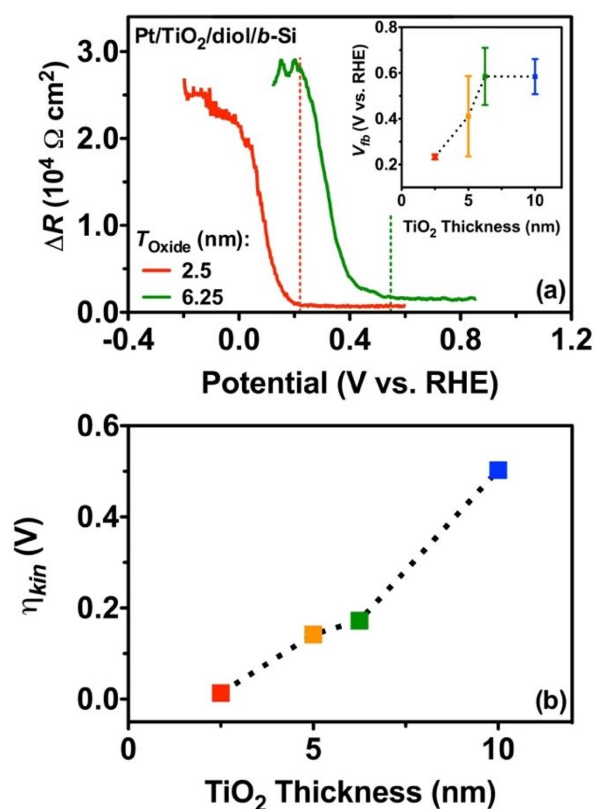


**Fig. 4** (a) Representative IMHFR plots of 'surface Pt' Pt/$TiO_2$ (*x* nm)/diol/*b*-Si where *x* = 2.5 nm (red) and 6.25 nm (green). The inset depicts $V_{fb}$ of samples where *x* = 2.5, 5, 6.25, and 10 nm. (b) $\eta_{kin}$ ($V_{fb} - V_{onset}$) of the samples shown in (a).

Accordingly, the energetic pathway from the $TiO_2$ to solution may be uphill, forming a thermodynamic pocket within the $TiO_2$ that grows deeper (hindering charge transfer) with increasing $TiO_2$ thickness. Ultimately, these results show that an interplay exists between the thermodynamics and electron transfer kinetics of the solution|Pt|$TiO_2$|diol|Si junction. Interestingly, $V_{fb}$ of the 15 nm samples could not be measured as no features were visible in the IMHFR plot. This phenomenon will be the subject of further study but may be a result of carriers moving into the $TiO_2$ too quickly to be detected by IMHFR or effectively blocking charge transfer when the $TiO_2$ is thick.

**Electrochemical Characterization of the Buried Pt Architecture**

We next explored the effect of depositing the diol/$TiO_2$ organic/inorganic hybrid architecture around Pt NPs buried deep within the silicon surface. In this way, we hypothesized that an oxide thickness might be found where the beneficial thermodynamics effects of $TiO_2$ are achieved without fully blocking the electrolyte|Pt interface, thereby maximizing $V_{fb}$ and minimizing $\eta_{kin}$. First, we found that 10–15 nm thick $TiO_2$ results in a large and negative $V_{onset}$, presumably due to the solution|Pt contact becoming partially or completely blocked by the $TiO_2$; indeed, ca. 5 voltammetric scans uncovered the Pt and achieved stable photoelectrochemical behaviour (full details on these observations can be found in the Supporting Information Figure S3 and associated discussion). We then conducted a combined voltammetry/IMFHR $TiO_2$ thickness-dependent electrochemical analysis for the 'buried Pt' samples to compare these to the 'surface Pt' electrodes. Figure 5 depicts the measured $V_{onset}$ (a) and $V_{fb}$ (b) values in addition to the calculated $\eta_{kin}$ (c). Contrary to the 'surface Pt' architecture, increasing $TiO_2$ thickness in the 'buried Pt' architecture shifts $V_{onset}$ positively until 15 nm $TiO_2$ where a small decrease relative to 10 nm is observed (Figure 5a inset; cf. Figure 3b). Interestingly, while deposition of 2.5 nm $TiO_2$ provides ~0.1 V positive shift in $V_{fb}$ relative to the $TiO_2$-free case, additional $TiO_2$ beyond 2.5 nm has no effect on $V_{fb}$ (Figure 5b). The possibility of Fermi energy pinning is ruled out (see next section below). Despite the insensitivity in $V_{fb}$ with $TiO_2$ thickness, the kinetic overpotentials ($\eta_{kin}$) decrease with increasing $TiO_2$ thickness up to 6.25 nm before increasing again for the 10 nm sample (Figure 5c). This is easily explained since the 'buried Pt' architecture likely subverts the kinetic limitations we describe in the 'surface Pt' case where the clean Si|Pt contact in the former allows for an unimpeded carrier transport pathway. A less intuitive but intriguing observation is that there is still a kinetic benefit from increased $TiO_2$ thickness despite this direct Si|Pt pathway. We speculate that the photoexcited electrons may move to the $TiO_2$ conduction band before migrating to the Pt NPs, limiting recombination with the holes that remain in the silicon. We also studied the durability of this architecture under sustained potentiostatic operation at 0 V vs RHE. As shown in Figure S5 for the 6.25 nm $TiO_2$ thickness sample, the current initially increases during the first 5 min before decaying over the next 30 min. The initial improvement in photocurrent is consistent with the $TiO_2$ dissolution we discuss above. The decay may be due to oxidation of the silicon underneath the buried NPs,



Please do not adjust margins

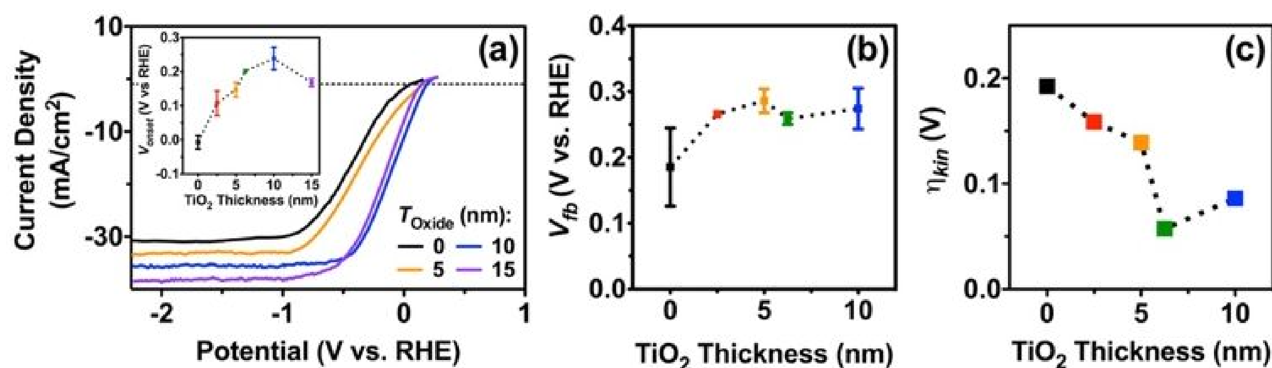


**Fig. 5** Energetics characterization of *x* nm 'buried Pt' $TiO_2$/diol/B-Pt/*b*-Si samples where *x* = 0, 2.5, 5, 6.25, 10, and 15 nm: (a) most positive $V_{onset}$ from voltammograms, (b) $V_{fb}$ from IMHFR plots, and (c) the calculated $\eta_{kin}$ value.

increasing the electron transfer overpotential. We observed similar oxidation of the underlying silicon during sustained photoelectrochemical operation of B-Pt/*b*-Si passivated with a native oxide.[49] Another possibility is silicon oxidation from photogenerated holes originating within the $TiO_2$.

**Fermi Pinning**

We were interested in further studying the relative insensitivity of $V_{fb}$ on $TiO_2$ thickness in the 'buried Pt' architecture since this could indicate the direct Si|Pt contact causes Fermi energy pinning. The thickness-dependent IMHFR characterizations for both interfacial architectures are shown in the Supporting Information (Figure S6). Our previous investigations on the diol- and $TiO_2$-free B-Pt/*b*-Si system so any indication that the diol or $TiO_2$ pins the Fermi energy would be an unusual result. To test whether the interface was in fact pinned, we collected IMHFR data in a series of buffered methyl viologen solutions for both architectures. As is widely known, the pH-dependence of oxidized surfaces is attributed to amphoteric sites at the surface, shifting the Helmholz potential based on the difference between the oxide isoelectric point and the solution pH.[1,59,60] Therefore, the energetics of the entire interface must adjust to the additional field and $V_{fb}$ of an unpinned junction will shift negatively with increasing pH. The pH-independent methyl viologen redox energy standardizes the solution redox potential while allowing the pH to change. If the energetics of the interface were pinned, little pH-dependence would be observed as the semiconductor interface instead equilibrates with (pinned) interfacial states, not the solution potential.

As shown in Figure 6, we observe pH-dependent shifts in $V_{fb}$ for *both* 'surface Pt' and 'buried Pt' architectures, conclusively demonstrating that neither architecture is Fermi energy pinned. Both electrodes exhibit a –36 mV/pH unit slope, similar to the –44 mV/pH unit slope previously observed on oxidized planar silicon.[61] Further, the $V_{fb}$ of the 'surface Pt' electrode is ~50 mVmore positive than that of the 'buried Pt' over all pH values tested (3–11), consistent with our previous observations. We conclude that when the Pt is deposited on top of the $TiO_2$, the Si|diol|$TiO_2$ interface is the predominant contact and $V_{fb}$ increases. Previous work demonstrates the thermodynamic (and kinetic) benefits of semiconductor|$TiO_2$ contacts and find similar shifts.[3] Alternatively, when the Pt is buried into the silicon, the deep Si|Pt contact supersedes the surface $TiO_2$ layer's thermodynamic effects.

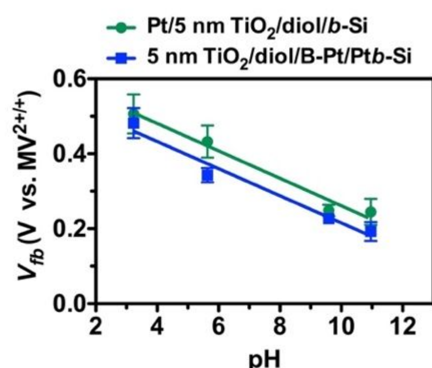


**Fig. 6** $V_{fb}$ function of pH (buffered solutions + 0.25 M $K_2SO_4$ + 50 mM methyl viologen).

## Conclusions

In this study we probed the relationships between interfacial architecture and energetics at the nanoporous black silicon surface. We made use of the hybrid organic/inorganic scheme to build a controlled silicon/molecular layer/metal oxide junction. The successful formation of a 1,4-butanediol surface monolayer was confirmed via cyclic voltammetry after a secondary binding of ferrocenecarboxylic acid redox reporter molecule. We measured considerably more ferrocene on the surface after diol functionalization, confirming the molecule is both present and available for secondary reactions (particularly nucleating $TiO_2$ during ALD). Interestingly, we find the presence of Pt on the surface limits ferrocene (and by extension diol) coverage by ~50%. The organic monolayer on the silicon was then used to nucleate $TiO_2$ deposited via ALD, on which Pt NPs additionally could be deposited.

The 'surface Pt' Pt/$TiO_2$/diol/*b*-Si architecture exhibits positive $V_{onset}$ values when the oxide layer is thin, but thicker


This journal is © The Royal Society of Chemistry 20xx

layers shifted $V_{onset}$ negatively. Investigation via IMHFR revealed this shift occurs despite the positively shifting $V_{fb}$, and the kinetic overpotential is severely limiting when the $TiO_2$ is thick. In contrast, in the 'buried Pt' $TiO_2$/diol/B-Pt/*b*-Si architecture increasing $TiO_2$ thickness only minimally modulates the thermodynamics as well as the kinetic overpotential owing to the direct Si|Pt contact in this system. We do not observe Fermi pinning of either interface. Importantly, we find the 'buried Pt' architecture circumvents the large kinetic overpotential observed when electrons are required to travel through thick $TiO_2$ as the 'surface Pt' hybrid interfacial system. However, placing the Pt on top of the oxide in this 'surface Pt' system allows for the formation of a thermodynamically favorable interfacial junction. These results suggest careful consideration of interfacial architecture is critical to optimal semiconductor junctions. A combined study using conventional votammetry along with IMHFR provides valuable insights that can be used to understand and inform new, complex interfacial architectures.

## Conflicts of interest

There are no conflicts to declare.

## Acknowledgements

This work was conducted by all authors, employees of the Alliance for Sustainable Energy, LLC, the manager and operator of the National Renewable Energy Laboratory for the U.S. Department of Energy (DOE) under Contract No. DE-AC36-08GO28308. Funding was provided by the U.S. DOE, Office of Science, Office of Basic Energy Sciences, Division of Chemical Sciences, Geosciences, and Biosciences, Solar Photochemistry Program. RTP was supported in part by the U.S. Department of Energy, Office of Science, Office of Basic Energy Sciences under the Science Graduate Student Research (SCGSR) fellowship program administered by the Oak Ridge Institute for Science and Education (ORISE) for DOE under contract number DE-SC0014664.

## References

1 R. van de Krol, in *Photoelectrochemical Hydrogen Production*, eds. R. van de Krol and M. Gratzel, Springer, New York, 2012, pp. 13–68.
2 D. G. Boucher, J. R. Speller and M. J. Rose, *Submitted.*
3 Y. Yang, J. Gu, J. L. Young, E. M. Miller, J. A. Turner, N. R. Neale and M. C. Beard, *Science*, 2015, **350**, 1061–5.
4 H. J. Kim, K. L. Kearney, L. H. Le, Z. J. Haber, A. A. Rockett and M. J. Rose, *J. Phys. Chem. C*, 2016, **120**, 25697–25708.
5 Y. W. Chen, J. D. Prange, S. Dühnen, Y. Park, M. Gunji, C. E. D. Chidsey and P. C. McIntyre, *Nat. Mater.*, 2011, **10**, 539–544.
6 S. Hu, M. H. Richter, M. F. Lichterman, J. Beardslee, T. Mayer, B. S. Brunschwig and N. S. Lewis, *J. Phys. Chem. C*, 2016, **120**, 3117–3129.
7 J. Gu, Y. Yan, J. L. Young, K. X. Steirer, N. R. Neale and J. A. Turner, *Nat. Mater.*, 2015, **15**, 456–460.
8 S. Hu, M. R. Shaner, J. A. Beardslee, M. Lichterman, B. S. Brunschwig and N. S. Lewis, *Science.*, 2014, **344**, 1005–1009.
9 H. J. Kim, K. L. Kearney, L. H. Le, R. T. Pekarek and M. J. Rose, *ACS Appl. Mater. Interfaces*, 2015, **7**, 8572–8584.
10 T. Moehl, J. Suh, L. Sévery, R. Wick-Joliat and S. D. Tilley, *ACS Appl. Mater. Interfaces*, 2017, **9**, 43614–43622.
11 R. T. Pekarek, K. Kearney, B. M. Simon, E. Ertekin, A. A. Rockett and M. J. Rose, *J. Am. Chem. Soc.*, 2018, **140**, 13223–13232.
12 B. Seger, T. Pedersen, A. B. Laursen, P. C. K. Vesborg, O. Hansen and I. Chorkendorff, *J. Am. Chem. Soc*, 2013, **135**, 1057.
13 Y. Lin, R. Kapadia, J. Yang, M. Zheng, K. Chen, M. Hettick, X. Yin, C. Battaglia, I. D. Sharp, J. W. Ager and A. Javey, *J. Phys. Chem. C*, 2015, **119**, 2308–2313.
14 D. Eisenberg, H. S. Ahn and A. J. Bard, *J. Am. Chem. Soc.*, 2014, **136**, 14011–14014.
15 H. H. Pham and L.-W. Wang, *Phys. Chem. Chem. Phys.*, 2015, **17**, 541–550.
16 T. Yao, R. Chen, J. Li, J. Han, W. Qin, H. Wang, J. Shi, F. Fan and C. Li, *J. Am. Chem. Soc.*, 2016, **138**, 13664–13672.
17 J. Aarik, J. Karlis, H. Mändar, T. Uustare and V. Sammelselg, *Appl. Surf. Sci.*, 2001, **181**, 339–348.
18 L. E. Garner, K. X. Steirer, J. L. Young, N. C. Anderson, E. M. Miller, J. S. Tinkham, T. G. Deutsch, A. Sellinger, J. A. Turner and N. R. Neale, *ChemSusChem*, 2017, **10**, 767–773.
19 J. Seo, H. J. Kim, R. T. Pekarek and M. J. Rose, *J. Am. Chem. Soc.*, 2015, **137**, 3173–3176.
20 R. K. Hiremath, M. K. Rabinal, B. G. Mulimani and I. M. Khazi, *Langmuir*, 2008, **24**, 11300–11306.
21 N. T. Plymale, A. A. Ramachandran, A. Lim, B. S. Brunschwig and N. S. Lewis, *J. Phys. Chem. C*, 2016, **120**, 14157–14169.
22 S. Maldonado, K. E. Plass, D. Knapp and N. S. Lewis, *J. Phys. Chem. C*, 2007, **111**, 17690–17699.
23 Y. Li, L. E. O'Leary, N. S. Lewis and G. Galli, *J. Phys. Chem. C*, 2013, **117**, 5188–5194.
24 D. C. Gleason-Rohrer, B. S. Brunschwig and N. S. Lewis, *J. Phys. Chem. C*, 2014, **117**, 18031–18041.
25 I. Yahyaie, S. Ardo, D. R. Oliver, D. J. Thomson, M. S. Freund and N. S. Lewis, *Energy Environ. Sci.*, 2012, **5**, 9789–9794.
26 R. T. Pekarek, H. Celio and M. J. Rose, *Langmuir*, 2018, **34**, 6328–6337.
27 L. J. Webb and N. S. Lewis, *J. Phys. Chem. B*, 2003, **107**, 5404–5412.
28 E. J. Nemanick, P. T. Hurley, L. J. Webb, D. W. Knapp, D. J. Michalak, B. S. Brunschwig and N. S. Lewis, *J. Phys. Chem. B*, 2006, **110**, 14770–14778.
29 J. J. Gooding and S. Ciampi, *Chem. Soc. Rev. Chem. Soc. Rev*, 2011, **40**, 2704–2718.
30 L. A. Huck and J. M. Buriak, *Langmuir*, 2012, **28**, 16285–16293.
31 F. Wu, W. Tian, F. Cao, L. Meng and L. Li, *ACS Appl. Energy Mater.*, 2018, **1**, 1286–1293.
32 C. R. Cabrera and H. D. Abruña, *J. Electroanal. Chem. Interfacial Electrochem.*, 1986, **209**, 101–107.

33 M. Wang, Y. Yang, J. Shen, J. Jiang and L. Sun, *Sustain. Energy Fuels*, 2017, **1**, 1633–1848.
34 J. J. Leung, J. Warnan, D. H. Nam, J. Z. Zhang, J. Willkomm and E. Reisner, *Chem. Sci.*, 2017, **8**, 5172–5180.
35 H. J. Kim, J. Seo and M. J. Rose, *ACS Appl. Mater. Interfaces*, 2016, **8**, 1061–1066.
36 J. Seo, R. T. Pekarek and M. J. Rose, *Chem. Commun.*, 2015, **51**, 4–7.
37 M. R. Nellist, F. A. L. Laskowski, F. Lin, T. J. Mills and S. W. Boettcher, *Acc. Chem. Res.*, 2016, **49**, 733–740.
38 O. S. Kang, J. P. Bruce, D. E. Herbert and M. S. Freund, *ACS Appl. Mater. Interfaces*, 2015, **7**, 26959–26967.
39 N. Tajimi, H. Sano, K. Murase, K. H. Lee and H. Sugimura, *Langmuir*, 2007, **23**, 3193–3198.
40 E. A. Dalchiele, A. Aurora, G. Bernardini, F. Cattaruzza, A. Flamini, P. Pallavicini, R. Zanoni and F. Decker, *J. Electroanal. Chem.*, 2005, **579**, 133–142.
41 F. Li, V. M. Basile and M. J. Rose, *Langmuir*, 2015, **31**, 7712–7716.
42 Q. Li, G. Mathur, S. Gowda, S. Surthi, Q. Zhao, L. Yu, J. S. Lindsey, D. F. Bocian and V. Misra, *Adv. Mater.*, 2004, **16**, 133–137.
43 F. Decker, F. Cattaruzza, C. Coluzza, A. Flamini, A. G. Marrani, R. Zanoni and E. A. Dalchiele, *J. Phys. Chem. B*, 2006, **110**, 7374–7379.
44 F. Li, V. M. Basile, R. T. Pekarek and M. J. Rose, *ACS Appl. Mater. Interfaces*, 2014, **6**, 20557–20568.
45 B. Fabre, *Chem. Rev.*, 2016, **116**, 4808–4849.
46 L. E. O'Leary, N. C. Strandwitz, C. W. Roske, S. Pyo, B. S. Brunschwig and N. S. Lewis, *J. Phys. Chem. Lett.*, 2015, **6**, 722–726.
47 J. Oh, T. G. Deutsch, H.-C. Yuan and H. M. Branz, *Energy Environ. Sci.*, 2011, **4**, 1690.
48 Y. Zhao, N. C. Anderson, K. Zhu, J. A. Aguiar, J. A. Seabold, J. Van De Lagemaat, H. M. Branz, N. R. Neale and J. Oh, *Nano Lett.*, 2015, **15**, 2517–2525.
49 J. A. Aguiar, N. C. Anderson and N. R. Neale, *J. Mater. Chem. A*, 2016, **4**, 8123–8129.
50 K. Sun, S. Shen, Y. Liang, P. E. Burrows, S. S. Mao and D. Wang, *Chem. Rev.*, 2014, **114**, 8662–719.
51 N. C. Anderson, G. M. Carroll, R. T. Pekarek, S. T. Christensen, J. Van De Lagemaat and N. R. Neale, *J. Phys. Chem. Lett.*, 2017, **8**, 5253–5258.
52 G. M. Carroll, R. Limpens and N. R. Neale, *Nano Lett.*, 2018, **18**, 3118–3124.
53 R. Zanoni, A. Aurora, F. Cattaruzza, C. Coluzza, E. A. Dalchiele, F. Decker, G. Di Santo, A. Flamini, L. Funari and A. G. Marrani, *Mater. Sci. Eng. C*, 2006, **26**, 840–845.
54 R. Zanoni, F. Cattaruzza, C. Coluzza, E. A. Dalchiele, F. Decker, G. Di Santo, A. Flamini, L. Funari and A. G. Marrani, *Surf. Sci.*, 2005, **575**, 260–272.
55 Y. Zhao, N. C. Anderson, M. W. Ratzloff, D. W. Mulder, K. Zhu, J. A. Turner, N. R. Neale, P. W. King and H. M. Branz, *ACS Appl. Mater. Interfaces*, 2016, **8**, 14481–14487.
56 J. Oh, H.-C. Yuan and H. M. Branz, *Nat. Nanotechnol.*, 2012, **7**, 743–748.
57 L. M. Wheeler, N. C. Anderson, P. K. B. Palomaki, J. L. Blackburn, J. C. Johnson and N. R. Neale, *Chem. Mater.*, 2015, **27**, 6869–6878.
58 R. C. Rossi and N. S. Lewis, *J. Phys. Chem. B*, 2001, **105**, 12303–12318.
59 A. J. Nozik, *Annu. Rev. Phys. Chem.*, 1978, **29**, 189–222.
60 H. Gerischer, *Electrochim. Acta*, 1989, **34**, 1005–1009.
61 E. L. Warren, S. W. Boettcher, M. G. Walter, H. A. Atwater and N. S. Lewis, *J. Phys. Chem. C*, 2011, **115**, 594–598.


This journal is © The Royal Society of Chemistry 20xx